CHEMISTRY OF MATERIALS

Article

Cite This: Chem. Mater. XXXX, XXX, XXX−XXX

pubs.acs.org/cm

Supercolossal Uniaxial Negative Thermal Expansion in Chloranilic Acid Pyrazine, CA-Pyz

Huiyu Liu,[†] Matthias J. Gutmann,[‡] Harold T. Stokes,[§] Branton J. Campbell,[§] Ivana Radosavljevic Evans,*[,†] and John S. O. Evans*[,†]

[†]Department of Chemistry, Durham University, Science Site, Durham DH1 3LE, U.K.

[‡]ISIS Neutron and Muon Source, Science and Technology Facilities Council (STFC) Rutherford Appleton Laboratory, Harwell Science and Innovation Campus, Chilton, Didcot, Oxfordshire OX11 0QX, U.K.

[§]Department of Physics & Astronomy, Brigham Young University, Provo, Utah 84602, United States

Ⓢ *Supporting Information*

ABSTRACT: There has been significant recent interest in exploiting the large dimension changes that can occur in molecular materials as a function of temperature, stress, or under optical illumination. Here, we report the remarkable thermal expansion properties of chloranilic acid pyrazine co-crystals. We show that the compound shows uniaxial negative thermal expansion over a wide temperature range with a linear contraction coefficient as low as $(-)1500 \times 10^{-6}$ K^{-1} at 250 K. The corresponding 10% contraction between 200 and 300 K is an order of magnitude larger than in the so-called colossal contraction materials. We adopt a symmetry-inspired approach to describe both the structural changes that occur (using rotational symmetry modes) and the thermal expansion (using strain modes). This allows an extremely compact description of the phase transition responsible for this unusual behavior and gives detailed understanding of its atomic origins. We show how the coupling of primary and secondary strain modes in materials showing extreme expansion and contraction can lead to unusual reversals in the temperature dependence of cell parameters.

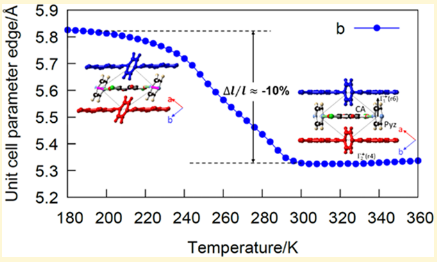

■ INTRODUCTION

There has been significant interest in the physical properties of crystalline organic and hybrid materials in recent years, particularly in some of the mechanical properties traditionally studied in metallic, ceramic, and polymer engineering materials.[1,2] The weaker bonding interactions present between organic molecules often enhance the magnitude of important properties, and their design-flexibility makes them a rich arena for discovery. Much of the interest in the field is driven by the possibility of creating stimulus-responsive materials that display macroscopic changes and can act as actuators or artificial muscles.[3−5]

For example, there has been a number of reports over the years of "bending crystals", which undergo dramatic shape changes either on heating or on the application of mechanical stress, some of which have been recently reviewed.[3,4] This behavior is usually linked to the evolution of twin structures associated with phase transitions and, as such, closely related to the phenomena that lead to effects such as shape memory and superelasticity in metal alloys like nitinol. There has, therefore, been significant interest in martensite-like transitions in organic crystals;[6−12] recent examples of materials exploiting these include the superelastic terephthalamide[13] and the organic shape memory material $(P^{n}Bu_4)^{+}(BPh_4)^{-}$.[14] Mechanical twinning leads to effects such as ferroelasticity and superelasticity, and a number of molecular systems have been reported with this property.[15−21] Finally, *N*,*N*-dimethyl-4-nitroaniline crystals have recently been shown to display superplasticity.[22] Herbstein provides a useful overview of the mechanism of organic transformations in the solid state, in particular summarizing the classic works of Ubbelohde and Mnyukh.[23]

The weaker interactions in molecular materials can also lead to more extreme behavior under changes in temperature than in conventional materials. This is exemplified by so-called negative thermal expansion (NTE) materials, which show the unusual property of contracting in volume on heating.[24] Most of the "classic" phonon-driven oxide NTE systems such as ZrW_2O_8,[25] $Sc_2(WO_4)_3$,[26] and zeolites[27] have negative linear contraction coefficients that are of comparable magnitude to the positive coefficients of normal materials ($\alpha_l \approx -20{-}0 \times 10^{-6}$ K^{-1}). ZrW_2O_8, for example, has $\alpha_l = -9 \times 10^{-6}$ K^{-1} from 2 to 300 K corresponding to a percentage contraction $\Delta l/l \approx -0.1\%$ over a 100 K range.[28] The term "colossal negative thermal expansion" was introduced to define materials with α_l more negative than -100×10^{-6} K^{-1} and hence a $\Delta l/l$ contraction larger than 1% over 100 K. The first such material was $Ag_3[Co(CN)_6]$, which showed a uniaxial NTE of -130×10^{-6} K^{-1}; this extreme contraction is related to the inherent flexibility of its framework structure, in which the volume is defined by a weak Ag−Ag argentophilic interaction.[29] In essence, this soft interaction leads

Received: March 21, 2019
Revised: May 27, 2019
Published: May 28, 2019

DOI: 10.1021/acs.chemmater.9b01135
Chem. Mater. XXXX, XXX, XXX−XXX

to a large positive expansion in two dimensions, with the framework topology driving a contraction along the perpendicular direction. Colossal isotropic NTE was subsequently reported in other framework systems such as the UiO-66 MOF.[30] Mullaney et al. have also shown how spin crossover can switch the geometry of flexible frameworks; by spin dilution, they could prepare materials with continuous cell parameter changes of +6/−4% over a 60 K range. This is strongly reminiscent of the major "breathing" changes in the geometry of metal organic frameworks such as MIL-5 on gas uptake.[31]

Extreme thermal expansion or contraction coefficients are also found in purely organic crystals where weaker intermolecular forces dominate. Some of the most dramatic are in the thermosalient[3,32] or "jumping crystals" such as (phenylazophenyl) palladium hexafluoroacetylacetonate[33] with α_a = +260.4 × 10^{-6} K^{-1} between 223 and 348 K and N'-2-propylidene-4-hydroxybenzohydrazide,[34] with $\alpha_{a/b} \approx +230 \times 10^{-6}$ K^{-1} and $\alpha_c \approx -290 \times 10^{-6}$ K^{-1} over the temperature range 298−373 K. (*S*,*S*)-octa-3,5-diyne-2,7-diol[35] has been reported as a biaxial NTE material with $\alpha_a = +450 \times 10^{-6}$ K^{-1}, $\alpha_b = -130 \times 10^{-6}$ K and $\alpha_c = -250 \times 10^{-6}$ K^{-} giving a relatively low overall volume expansion α_V = +60 × 10^{-6} K^{-1} (all 240−330 K). Methanol monohydrate, in contrast, has a large volume expansion α_V = +500 × 10^{-6} K^{-1} that causes a more modest contraction in one dimension $\alpha_a = -60 \times 10^{-6}$ K^{-1} (both at 155 K) along with negative linear compressibility.[36]

Here, we report the remarkable thermal expansion properties of a chloranilic acid pyrazine (CA-Pyz) co-crystal associated with a newly-discovered phase transition. The molecular structure and views of the three-dimensional packing (which will be discussed in detail later in the text) are shown in Figure 1.

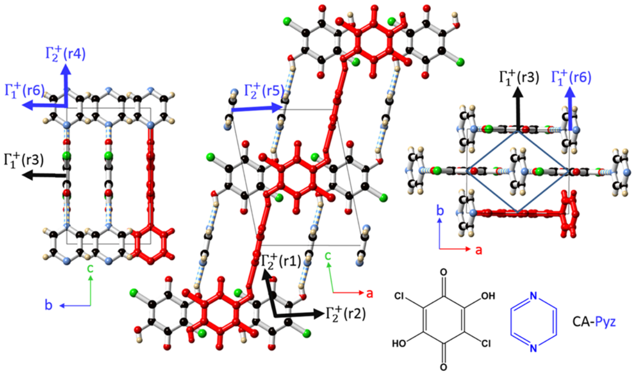

Figure 1. Molecular structure of chloranilic acid (CA) and pyrazine (Pyz), and views of the CA-Pyz co-crystal structure at 300 K along *a*, *b*, and *c* (left to right). The monoclinic high-temperature (HT) unit cell is shown in gray. The bold blue "diamond" in the view of the *ab* plane shows the low-temperature triclinic cell discussed in the text and used for most analysis. Heavy black and blue arrows show directions of rotational symmetry modes for CA and Pyz, respectively. A chain of hydrogen-bonded CA-Pyz molecules is highlighted in red.

Powder and single-crystal diffraction studies have shown that this material undergoes a phase transition which leads to extreme distortions of its unit cell. Its volume change from 200 to 300 K is one of the largest known for an organic crystal, and it shows extreme anisotropy in the contraction and expansion of its *a* and *b* cell parameters. Average linear thermal expansion coefficients approaching ±1000 × 10^{-6} K^{-1} are observed from 200 to 300 K corresponding to 10% length changes, an order of magnitude larger than required by the definition of "colossal". Our structural studies and the application of rigid-body rotational symmetry modes allow us to understand and describe the molecular origins of this fascinating behavior. We also present a simple model to explain the unusual temperature evolution of cell parameters that can arise in materials showing such extreme thermal expansion.

EXPERIMENTAL SECTION

Sample Preparation. Single crystals of CA-Pyz were obtained by slow evaporation of an acetonitrile solution of chloranilic acid (Aldrich, 98%) and pyrazine (Aldrich, 99%) in a 1:1 molar ratio. Chloranilic acid (0.0627 g, 0.3 mmol) and pyrazine (0.0240 g, 0.3 mmol) were dissolved separately in the minimum volume of acetonitrile (typically 6 and 1 mL, respectively) with gentle heating for 30 min. Orange-red rhombus-shaped crystals appeared after 2 days. Polycrystalline samples were produced by gentle grinding of crystals.

Single-Crystal Diffraction. Single-crystal X-ray diffraction data were acquired on an Oxford Gemini S Ultra diffractometer equipped with a CCD area detector, using Mo Kα radiation (λ = 0.71073 Å). Data were collected at 300, 275, 250, 230, 200, and 150 K on both cooling and warming. A Cryostream Plus Controller was used to control the experimental temperature. Crystal structures were solved using SIR92[37] within the CRYSTALS[38] software. All nonhydrogen atoms were refined anisotropically against F_{hkl}^2. All hydrogen atoms were located by difference Fourier maps and refined isotropically without any restraints. Single-crystal neutron diffraction data were collected on the SXD instrument of the ISIS Neutron and Muon Source at the Rutherford Appleton laboratory. The crystal was attached to a goniometer head using adhesive Al foil and placed in a rotating bottom-loading CCR. Data were collected at 295 K, in 10 crystal orientations for 3 h each. Initial data reduction was done using the SXD2001 software within the IDL virtual machine, and refinement of the structural model was carried out in Jana2006.[39] The fractional coordinates and anisotropic atomic displacement factors were refined for all atoms against F_{hkl}^2. Translation, libration, screw (TLS) tensors were derived from experimental anisotropic displacement parameters in Platon.[40]

Powder Diffraction. Synchrotron powder X-ray diffraction data were collected at a beamline I11 at Diamond Light Source in high-resolution mode using the 45 Multi-Analysing Crystal detector and a wavelength λ = 0.8257653 Å (calibrated against a silicon standard NIST 640c). The sample was loaded into a 0.7 mm external-diameter quartz capillary to a length of 30 mm. The capillary was sealed and attached to a brass holder, which rotated during the measurements. Variable temperature data were collected every 4 K between 180 and 360 K. Laboratory powder X-ray diffraction data were collected in capillary mode on a Bruker D8 diffractometer equipped with a Lynx-Eye detector and an Oxford Cryosystems Cryostream Plus device, using Mo Kα radiation. The sample was warmed from 150 to 400 K at a rate of 15 K/h. A series of 20 min datasets were recorded over a 2θ range of 1−30° using a step size 0.01°. All powder diffraction data were analyzed using the TOPAS Academic software.[41−43]

Solid-State NMR and Thermal Analysis. ^{1}H solid-state NMR was recorded at 205 and 308 K with a 15 kHz spinning rate on a Bruker Advance III HD instrument. Differential scanning calorimetry (DSC) experiments were performed on a PerkinElmer Pyris 1 DSC instrument. The sample (2.831 mg) was heated from 120 to 520 K at rates between 10 and 100 K/min.

Symmetry-Mode Analysis. Symmetry-adapted distortion modes belonging to the irreducible representations of the parent-symmetry group, commonly referred to as "symmetry modes", were employed here to describe global patterns of rigid-body rotations. For brevity, we refer to such patterns simply as "rotational symmetry modes".

Rotational symmetry modes were defined for a dummy pivot atom placed at the center of inversion of each molecule. Command files containing both a rotational symmetry-mode description and a more familiar displacive symmetry-mode description were generated in a format suitable for TOPAS Academic. Rotational symmetry-mode amplitudes were refined directly using the laboratory powder diffraction data with displacive symmetry modes fixed at zero. Rotational

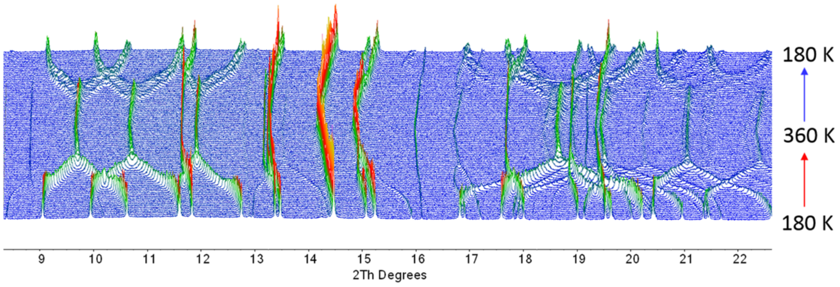

Figure 2. Pseudo-three-dimensional plot of synchrotron powder diffraction data ($\lambda = 0.8258$ Å) collected on CA-Pyz on warming from 180 to 360 and subsequent cooling back to 180 K.

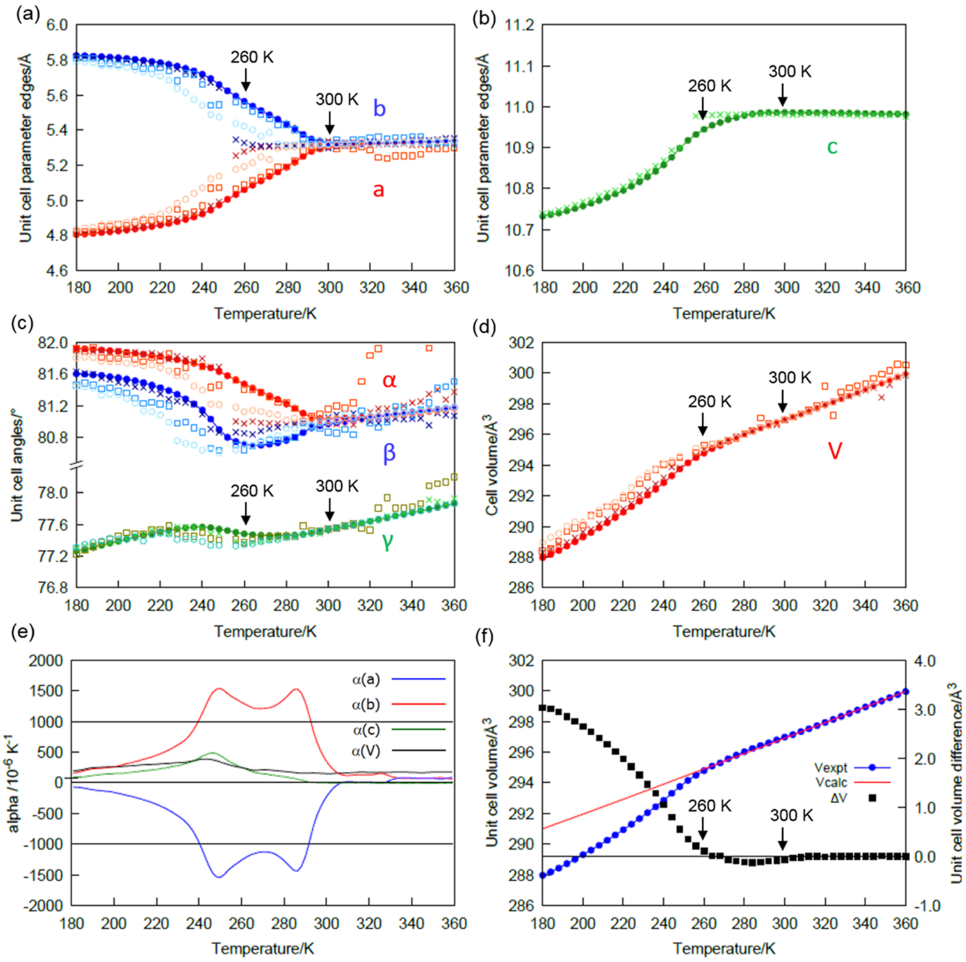

Figure 3. Unit cell parameters based on the triclinic cell (Figure 1, blue) extracted from powder data collected on warming (solid markers) and cooling (open markers and crosses). Data reveal some hysteresis and multiphase behavior just below the phase transition temperature on cooling. (a) Unit cell parameters *a* and *b*. (b) Unit cell parameter *c*. Note the very different *y*-axis scale of $\Delta l/l \approx 25\%$ and $\approx 5\%$ in (a) and (b). (c) Unit cell angles *α*, *β*, and *γ*. (d) Unit cell volume. (e) Thermal expansion coefficients for each unit cell axis; values derived by fitting a smooth function to the data shown in (a)−(d) followed by numerical differentiation. (f) Unit cell volume and volumetric strain relative to values extrapolated from high-temperature.

symmetry-mode amplitudes were extracted from single-crystal experiments by minimizing the distances between all atoms in a rotational symmetry-mode description with displacive symmetry-mode amplitudes fixed at zero (based on the 300 K single-crystal structure) and the conventionally refined fractional atomic coordinates. The sensitivity of extracted rotational symmetry-mode amplitudes to internal distortions of molecules was assessed by also refining displacive symmetry-mode amplitudes to give a perfect fit to the conventional coordinates but with displacive amplitudes restrained to values as close to zero as possible such that rotational symmetry modes described the majority of the atomic movement. All symmetry-mode calculations were performed using the ISODISTORT software.[44]

■ RESULTS AND DISCUSSION

Observation and Analysis of a Structural Phase Transition in CA-Pyz. Figure 2 shows powder diffraction data recorded on warming and subsequent cooling of CA-Pyz from 180 to 360 to 180 K (equivalent lab data used in Figure 4b are given in the Supporting Information (SI) Figure S1). It is immediately apparent from these data that CA-Pyz undergoes a phase transition at around 300 K, and the extreme splitting of certain *hkl* reflections suggests that the transition is associated with significant changes in the unit cell parameters. We see no

DOI: 10.1021/acs.chemmater.9b01135
Chem. Mater. XXXX, XXX, XXX−XXX

significant features in the DSC at this temperature, but this is perhaps unsurprising given the wide temperature range over which the transition occurs.

The 150 K data can be indexed with a triclinic unit cell with $a = 4.78$ Å, $b = 5.83$ Å, $c = 10.71$ Å, $\alpha = 82.0°$, $\beta = 81.5°$, $\gamma = 77.0°$, $V = 286$ Å^3. Figure 1 shows the relationship of this triclinic cell (bold blue lines) to the previously reported monoclinic high-temperature cell (gray lines). Figure 3 shows unit cell parameters extracted by Pawley fitting,[45] using both the warming and cooling datasets. On warming, we see some peak broadening just below the phase transition temperature T_C (300 K), which was modeled using just 4 of the 15 allowed terms of a 4th-order spherical harmonic to describe anisotropic microstrain.[41,46] The magnitudes of the coefficients obtained are included in the SI (Figure S2).

At high temperature, the Bragg peaks are essentially as sharp as at low temperature. On cooling, the phase transition is fully reversible, though there is a subtle thermal history-dependent splitting of some of the "tuning-fork" reflections just below the phase transition temperature. By tuning fork, we mean reflections such as the ∼9.5° 2θ peak ((11−1) at high T; (011) and (101) at low T), which undergo particularly marked splitting, resulting in the reflections that are equivalent at high temperature being separated by several degrees in 2θ at low temperature. The cooling data can be Pawley-fitted by using three closely related phases just below T_C, and we show their unit cell parameters as open points and crosses in Figure 3. Importantly, the sample regains sharp, essentially unstrained peaks at low temperature where the powder diffraction pattern can again be described using a single phase. This is demonstrated, for example, by the convergence of cell parameters of the three Pawley-fit phases to identical values at low temperature. Similar effects have been reported in other high-anisotropy systems such as MIL53[47,48] and could be caused by intergrain effects or the significant microstrain build-up between ∼220 and 300 K, which is shown in the SI (Figure S2).

Structure of the New (LT) Form of CA-Pyz. To gain detailed insight into the structural changes associated with the phase transition, single-crystal X-ray diffraction experiments were performed at 6 temperatures between 300 and 150 K (on both warming and cooling). The crystallographic parameters are summarized in Tables S1 and S2 and cell parameters plotted in Figure S3. At 300 K, CA-Pyz was found to adopt the previously reported monoclinic structure[49] in space group $C2/m$ with unit cell parameters of $a = 8.296(5)$ Å, $b = 6.654(2)$ Å, $c = 10.993(2)$ Å, $\beta = 101.60(3)°$ and $V = 594.44(11)$ Å^3. We refer to this as the high-temperature (HT) form of CA-Pyz. Below this temperature, a new triclinic form (LT form, space group $P\bar{1}$) was observed and its structure was solved from the 150 K data set. The molecular packing in the two forms is very similar, facilitated by a one-dimensional network of O−H···N hydrogen bonding (see Figure 5), which gives rise to the CA-Pyz chains highlighted in red in Figure 1. With the donor−acceptor distance of $d_{ON} \approx 2.7$ Å, these are medium-length O−H···N hydrogen bonds.[50] Using the C−O bond lengths (determined from X-ray diffraction more reliably than those involving hydrogen atoms) as a proxy for detecting potential temperature-induced proton migration, we find no evidence of this type of dynamics; these bond lengths remain at about 1.31 Å between 150 and 300 K (Figure S4), suggesting that the single bond character is retained throughout this temperature region.[51] Similarly, we see no evidence to suggest significant distortions of individual molecules.

Single-crystal neutron diffraction data recorded at 295 K allowed accurate determination of the hydrogen atom positions and anisotropic atomic displacement parameters (ADPs). A view of the ADPs at all temperatures is shown in Figure S5 and for the 295 K structure in Figure 5. The most striking structural feature is the magnitude and the orientation of the ADPs on the atoms in the pyrazine molecule. Ishida and Kashino[49] noted large anisotropic displacements of the C4 atom perpendicular to the pyrazine ring, but their attempts to model these by disordering the carbon atoms around a pseudo two-fold rotation axis passing through the N atoms (i.e., as static disorder) were not successful. This, together with our observation of large H-atom ADPs, suggests a very prominent librational motion perpendicular to the pyrazine ring at a high temperature. As an approximation, a translation, libration, screw (TLS) analysis of the experimental neutron ADPs[52] gives eigenvalues of the librational tensor of the Pyz molecule of ∼22, 8, and 6° and translations of 0.36, 0.23, and 0.1 Å^2.

Further evidence for the dynamics in the HT form of CA-Pyz comes from ^{1}H solid-state NMR data recorded at 205 and 308 K (Figure S6). Both OH and Pyz proton signals undergo significant narrowing on warming: from 950/1490 to 550/600 Hz, respectively. The CA OH chemical shift changes by ∼0.5 ppm indicating a minor change in the proton environment and hydrogen bond network between the two phases.

Rotational Symmetry-Mode Description of the Phase Transition in CA-Pyz. The power of using symmetry-adapted distortion modes belonging to the irreducible representations of the parent-symmetry group (a.k.a. symmetry modes) to describe the order parameters that arise in symmetry-reducing phase transitions is now widely appreciated.[44,53−56] Key advantages are that the essence of the phase transition can often be captured by a small number of parameters (mode amplitudes), each of which quantifies a structural distortion that breaks the parent symmetry in a unique way, and each of which is defined to be zero in the high symmetry parent phase. Symmetry-mode parameters, thus, tend to have clear physical interpretations and origins.

The full parameterization of an arbitrary crystal−crystal phase transition in terms of symmetry modes was initially accomplished for atomic displacements, which are polar vectors.[55−57] The group theoretical calculations required for the construction of displacive symmetry modes are available within the ISODISTORT software package.[44] ISODISTORT also includes symmetry modes to describe the ordering of atomic species (occupational order−disorder), magnetic moments (time-reversible axial vectors), and, most recently, rotational moments (non-time-reversed axial vectors). A rotational symmetry-mode approach can give a very compact description of an entire pattern of rotation vectors, where each vector rotates a group of atoms, such as a rigid molecule or polyhedral unit. Note that the three components of a molecular rotation vector capture the same information as would be specified by three rotational angles (e.g., around three orthogonal axes) in a conventional rigid-body description. The rotation vector is more convenient, because it can be directly visualized (see below) and because there are no arbitrary conventions to consider regarding the order of the rotations around different axes. A rotation vector's orientation defines the rotation axis, and its length defines the angle of rotation.[58]

These ideas have previously been applied to describe the low-symmetry structure of the extended solid $RbBr_3Mg(H_2O)_6$,[59] and, more recently, the unusual high-to-low-symmetry phase

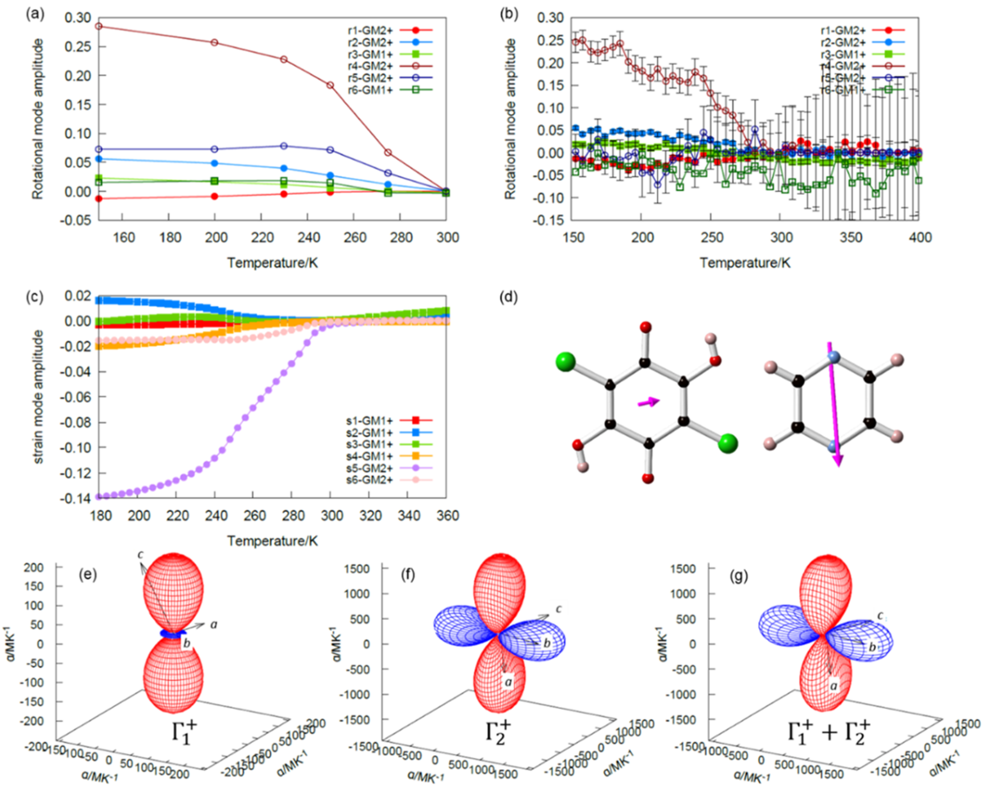

Figure 4. (a) Rotational symmetry-mode amplitudes r_1−r_3 (CA, shaded markers) and r_4−r_6 (Pyz, open markers) extracted from single-crystal refinements on warming; the effect of each rotation is shown in Figure 1. (b) Equivalent parameters from powder data. (c) Strain-mode amplitudes s_1−s_6 relative to the 300 K cell. (d) Rotation vectors for CA and Pyz; vectors length displayed as 1 Å = 8°. (e−g) Thermal expansion indicatrices for (e) Γ_1^+ only, (f) Γ_2^+ only, and (g) $\Gamma_1^+ + \Gamma_2^+$ strains between 250 and 300 K; red and blue indicate positive and negative, respectively; the scales in (f) and (g) are approximately an order of magnitude larger than (e).

transition (on warming) of the molecular ferroelectric 5,6-dichloro-2-methylbenzimidazole[60] and the cooperative motions of networks of interconnected rigid units.[61]

The refined structures from single-crystal diffraction experiments allow us to develop a straightforward description of the child LT phase of CA-Pyz in terms of the rotational symmetry modes belonging to the Γ_2^+ irrep of the parent HT phase. The Γ_2^+ irrep of space group $C2/m$ results in a $P\overline{1}$ subgroup of index 2 with basis {(1/2, 1/2, 0), (1/2, −1/2, 0), (0, 0, −1)}[62] and origin at (0,0,0) relative to the conventional parent cell (the blue cell of Figure 1). The child has 36 displacive symmetry modes (spanning the same space as the 36 free *xyz* atom-position parameters in the conventional description), 24 of which (the Γ_1^+ modes) describe structural degrees of freedom already present in the parent. Alternatively, if we assume rigid molecules, which merely rotate around their respective inversion centers, we need only consider 6 rotational symmetry modes (spanning the same space as the 6 free *xyz* components of the two molecular rotation vectors). The LT phase has a Γ_1^+ and two Γ_2^+ irrep modes for each molecule, which are illustrated in Figure 1. The $\Gamma_1^+Ag(a)$ modes (labeled r_3 and r_6 in Figure 1 and below) describe rotations around the parent *b* axis and are allowed degrees of freedom in the parent; the rotation axes associated with this mode are perpendicular to the CA molecular plane and in the Pyz molecular plane and perpendicular to the N−N vector. The symmetry-breaking $\Gamma_2^+Bg\_1(a)$ modes (r_1 and r_4) are rotations around the parent *c* axis and lie approximately parallel to the C═O bond of CA and the N−N vector of Pyz. The symmetry-breaking $\Gamma_2^+Bg\_1(b)$ modes (r_2 and r_5) are rotations around the parent *a* axis and are approximately perpendicular to the C═O axis of CA and to the Pyz plane.

For small rotations of rigid molecules, these 6 parameters should allow us to capture the key features of the phase transition. If additional molecular distortions occur, these can be described by refining additional displacive symmetry-mode amplitudes as internal degrees of freedom within the "semirigid" bodies. These internal modes can also be used to correct for distortions caused by large changes in cell metric when rigid bodies are defined using parent fractional coordinates. If one attempts to simultaneously use both 6 rotational symmetry modes and 36 displacive symmetry modes to describe the structure, then the description will, of course, be over-parameterized. This is corrected by removing 6 appropriate linear combinations of displacive symmetry modes that result in pure rotations. Alternatively, one can use soft restraints to keep unnecessary displacive symmetry-mode amplitudes close to zero during refinement, forcing the rotational symmetry modes to "do most of the work" in describing atomic coordinate shifts. We adopt this latter approach for part of our analysis.

Rotational symmetry-mode amplitudes, extracted by fitting the rotating rigid bodies (as defined using the 300 K high symmetry parent structure) to the refined conventional atomic coordinates from lower temperature single-crystal datasets, are shown in Figure 4a. Figure 4b shows equivalent mode amplitudes refined directly from relatively low-quality laboratory powder diffraction data. The good qualitative and quantitative agreement between Figure 4a and 4b shows that this restricted parameter set (in contrast to traditional *xyz* refinements) can be reliably extracted from low-quality

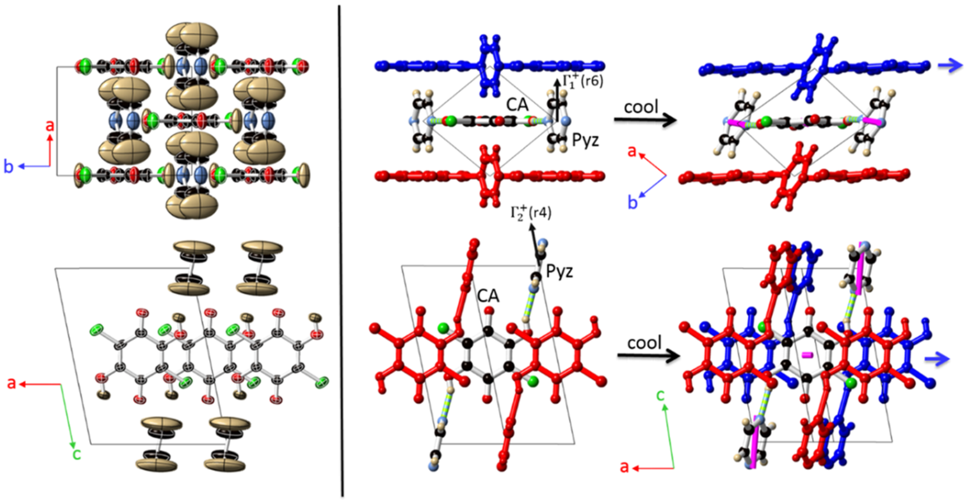

Figure 5. Relationship between the high- and low-temperature structures of CA-Pyz. Left-hand pictures show ADPs from 295 K neutron diffraction refinements using the monoclinic cell. Middle pictures show views down the *c*-axis (top) and perpendicular to planes of CA (bottom) at high temperature using the triclinic cell. Right-hand plots are equivalent views at low temperature. Pink cylinders represent the overall rotation of each molecule from high to low temperature; their length is proportional to the rotation angle. Blue arrows show the direction of movement of the corresponding CA-Pyz chain. Black arrows show directions of the important rotational symmetry modes.

laboratory powder diffraction data. We see from these plots that Γ_2^+ rotations (circles) have by far the highest magnitude and are, therefore, the most important in describing and understanding the phase transition. Pyz molecular rotations (open markers) are also much more important than those of the CA molecule (closed markers). Figure 4d displays the resulting rotation vectors for each molecule. For Pyz, we see that the large ∼16° rotation is almost aligned with the N−N vector. For CA, the smaller ∼4° rotation is approximately perpendicular to the C═O vector and slightly out of the molecular plane. We emphasize that the mode amplitudes of Figure 4a, or their simpler representation in Figure 4g, describe the structural changes that occur due to the phase transition. From the temperature dependence of r_4, we see that the effects of the transition are apparent from ∼150 to 300 K.

As with any rigid-body description, there are approximations in this approach such that the rigid-body coordinates will be slightly different to those from free refinement. Some differences arise from the fact that at high temperatures, the relatively rigid molecules undergo correlated vibrational motions leading to the well-known underestimation of bond lengths when using harmonic displacement parameters.[63] The magnitude of this effect can be appreciated from the left-hand panels of Figure 5, which show anisotropic displacement parameters extracted from neutron single-crystal diffraction refinements. These lead to the HT Pyz molecule showing shorter apparent bond lengths than at low temperature. Our TLS analysis of the neutron-derived structure gives observed and corrected C−N distances of 1.275 and 1.360 Å, respectively. These compare to bond lengths of 1.269 and 1.346 Å obtained from single-crystal X-ray data at 300 K and 150 K, respectively, confirming the librational shortening. Distortions due to the extreme changes in cell metric observed in this particular compound also lead to atoms being up to 0.1 Å from true positions in the molecular rotation description. If internal displacive symmetry-mode amplitudes are refined to give perfect atomic overlap with a restraint applied so that as much of the atomic displacements are captured by rotational symmetry modes as possible, the values of r_1 to r_6 (as shown in Figure 4a) change very little. The rotating rigid-body model, therefore, captures most of the key structural changes in a small number of parameters that can be routinely and reliably determined.

Remarkable Thermal Expansion Behavior of CA-Pyz. We can adopt a similar language to describe the cell parameter changes relative to 300 K that occur on cooling. This involves using strain modes, which transform as polar symmetrized second-rank tensors. The six degrees of freedom of the low-temperature cell appear as four parent-allowed Γ_1^+ strain modes (labeled here s_1−s_4) and two parent-symmetry-breaking Γ_2^+ modes (s_5 and s_6); their amplitudes are shown in Figure 4c. As expected, Γ_2^+ strains refine to essentially zero above $T_c = 300$ K for the monoclinic HT phase but show a marked deviation from 0 below 300 K, with the Γ_2^+ s_5 strain reaching a remarkable −0.14 (−14%) by 180 K. It also seems that the Γ_1^+ strains show a different temperature dependence than those of Γ_2^+ irrep, with significant deviations from their high-temperature extrapolated behavior only appearing below $T \approx 260$ K. The Γ_2^+ s_5 mode also displays a clear discontinuity at this lower temperature.

The influence of the strain modes on individual cell parameters depends on the cell setting used. To properly decouple the physical changes of the crystal from the cell setting, we have calculated thermal expansion along the principal axes of the expansion tensor. Figure 4e−g shows expansion indicatrices considering just Γ_1^+, just Γ_2^+, and $\Gamma_1^+ + \Gamma_2^+$ overall strains and their relationships to the parent cell axes. As anticipated from Figure 2, we see extremely large negative thermal expansion (blue) close to the parent *b*-axis, extremely large positive expansion (red) close to the *a*-axis, and more normal (though still large) positive expansion close to the *c*-axis. Average thermal expansion coefficients over a 200−300 and 250−300 K temperature range are given in Table 1, and their full temperature evolution is plotted in Figure 3e. We see that the extreme uniaxial contraction ($\alpha_l = -1500$ K^{-1} at 250 K) is dominated by Γ_2^+ strains, and that the dominant effect of Γ_1^+ is an expansion of the interlayer *c*-axis. If we use a nonstandard $C\bar{1}$ setting for the child structure, we, of course, see the same temperature dependence of strain modes, but they manifest in a different temperature dependence of cell parameters (see SI Figure S7 and discussion

DOI: 10.1021/acs.chemmater.9b01135
Chem. Mater. XXXX, XXX, XXX−XXX

Table 1. Irrep-Specific Thermal Expansions (left) over the 250−300 K range (200−300 K Values Given in Parentheses for $\Gamma_1^+ + \Gamma_2^+$), along Principal Axes X1−X3, Ordered from Lowest (X1) to Highest (X3) Values, and Overall Volume Expansion[a]

	thermal expansion (10^{-6} K^{-1}) along principal axes			principal-axis components for overall $\Gamma_1^+ + \Gamma_2^+$ expansion		
	Γ_1^+	Γ_2^+	$\Gamma_1^+ + \Gamma_2^+$	*a*	*b*	*c*
X1	−34	−1345	−1375 (−893)	−0.10	0.99	−0.07
X2	−33	−18	+196 (+188)	−0.17	0.01	0.99
X3	+205	+1552	+1524 (+1065)	−0.99	0.10	0.03
volume	+138	+88	+245 (+270)			

[a] Right-hand columns show each principal-axis direction relative to crystallographic axes for the overall strain (i.e., components of Xn directions along *a*, *b*, and *c*, as shown in Figure 4g). Estimated uncertainties on expansion coefficients are ~30 × 10^{-6} K^{-1}.

below). In this alternative description, the large −14% amplitude of the s_5 Γ_2^+ mode predominantly influences the cell angle γ, which changes from 90 to ~101.5° between 300 and 150 K.

The trigonometric dependencies of the individual child-cell parameters on the strain modes are considerably more complicated than that of the volume. However, we can expand these dependencies to first order and then apply the observed 150 K strain-mode amplitudes to determine which contributions are most important to the thermal expansion (Table 2). These approximations also help to rationalize the extremely unusual temperature dependencies of the cell parameters in Figure 3. For example, the unit cell angle β initially decreases on cooling through T_c but then increases below $T \approx 260$ K, whereas angle increases monotonically on cooling. When we look at which modes influence α and β, we see that they vary in opposite directions with respect to either mode s_5 or s_6 of Γ_2^+; the sensitivity to s_5 is weak and the amplitude of s_5 is large, whereas the sensitivity to s_6 is strong and the amplitude of s_6 is small. As a result, s_5 and s_6 end up making comparable angle changes of magnitudes 0.811 and 0.575° at 150 K. The total contributions of Γ_2^+ are then $\Delta\alpha = 0.811 - 0.575 = 0.236°$ and $\Delta\beta = -0.811 + 0.575 = -0.236°$. The sizeable amplitudes of modes s_2 and s_4 of Γ_1^+ must also be considered, especially due to the high sensitivity of both angles to s_2; the total contributions of Γ_1^+ strains are $\Delta\alpha = \Delta\beta = 1.019 - 0.199 = 0.820°$ at 150 K, which are ultimately much larger than those of Γ_2^+. The combined multiirrep contributions ($\Gamma_1^+ + \Gamma_2^+$) are then $\Delta\alpha = 0.820 + 0.236 = 1.056°$ and $\Delta\beta = 0.820 - 0.236 = 0.584°$ at 150 K. However, because the Γ_1^+ modes acquire significant amplitudes only well below the 300 K transition (Figure 4c), the Γ_2^+ decrease in $\Delta\beta$ with decreasing temperature is well underway, before the much larger Γ_1^+ increase in $\Delta\beta$ begins to evolve, resulting in the striking trend reversal observed.

Although less obvious from Figure 3d, similar effects are seen in the cell volume, which shows a marked discontinuity at 260 K and a smaller discontinuity at 300 K. This is more apparent in the plot of volumetric strain relative to that extrapolated from the HT structure in Figure 3f and the thermal expansion plots of $(1/a)\mathrm{d}a/\mathrm{d}T$ in Figure 3e. Unlike the individual cell parameters, the dependence of the cell volume on the strain amplitudes is relatively simple (a third-order multivariable polynomial)

$$\frac{\Delta V}{V} = s_1 + s_3 + s_4 + s_1s_3 + s_1s_4 + s_3s_4 + s_1s_3s_4 - \frac{1}{2}(s_2^2 + s_5^2 + s_6^2 + s_3s_2^2 + s_4s_5^2 + s_1s_6^2) + \frac{1}{\sqrt{2}}s_2s_5s_6$$

Considering only the lowest-order term in each strain (s_1, s_3, s_4, s_2^2, s_5^2, s_6^2), we see that the volume change is approximately linear in, and hence very sensitive to, strains s_1, s_3, s_4, which tend to operate primarily on the cell-edge lengths. In contrast, the volume change is merely quadratic in, and hence much less sensitive to, strains s_2, s_5, s_6, which tend to operate primarily on the cell angles. As a result, despite the fact that the Γ_2^+ strain s_5 dominates the structural (and presumably the energetic) changes, the much smaller Γ_1^+ strain s_4 makes the dominant contribution to the volume change.

It remains to explore why the primary Γ_2^+ strain modes and secondary Γ_1^+ strain modes evolve at such different temperatures. In this context, the word "secondary" implies the mathematical inability to generate the low-symmetry subgroup and hence the physical inability to drive the transition; in this case, the secondary modes do not break any parent symmetries at all since Γ_1^+ is also the identity irrep. One possible explanation is the occurrence of a second-phase transition near 260 K, which would necessarily be isosymmetric (space group $P\overline{1}$ is retained) and first order since its order parameter belongs to the identity irrep. We see no strong evidence to support such a phase transition in our data. In addition, a closer examination of Figure 4c reveals that the secondary Γ_1^+ modes exhibit small but nonzero departures from their high-temperature trends between 260 and 300 K. We, therefore, believe that the observed behavior is caused by a coupling between the primary Γ_2^+ and secondary Γ_1^+ order parameters. In essence, for strains as large as those observed in CA-Pyz, cross-coupling terms in the Landau free-energy expansion become sufficiently large that they can no

Table 2. First-Order Terms in the Expansion of Each Child-Cell Parameter (Å or Radian Units) in the Unitless Strain-Mode Amplitudes at 300 K, along with the Resulting Contributions at 150 K in Parentheses[a]

irrep	mode	Δa	Δb	Δc	$\Delta\alpha$	$\Delta\beta$	$\Delta\gamma$
Γ_1^+	s_1 (−0.0009)	3.234 s_1 (−0.003)	3.234 s_1 (−0.003)	0.444 s_1 (≈0)	−0.214 s_1 (≈0)	−0.214 s_1 (≈0)	−0.976 s_1 (0.049)
Γ_1^+	s_2 (0.0169)	0	0	−3.061 s_2 (−0.052)	1.050 s_2 (1.019)	1.050 s_2 (1.019)	0
Γ_1^+	s_3 (−0.0053)	2.082 s_3 (−0.011)	2.082 s_3 (−0.011)	0	0.062 s_3 (≈0)	0.062 s_3 (≈0)	0.976 s_3 (−0.295)
Γ_1^+	s_4 (−0.0228)	0	0	10.549 s_4 (−0.240)	0.152 s_4 (−0.199)	0.152 s_4 (−0.199)	0
Γ_2^+	s_5 (−0.1422)	3.670 s_5 (−0.522)	−3.670 s_5 (0.522)	0	0.071 s_5 (−0.575)	−0.072 s_5 (0.575)	0
Γ_2^+	s_6 (−0.01612)	0	0	0	−0.878 s_6 (0.811)	0.878 s_6 (−0.811)	0

[a] The values in a given column can be summed to determine the approximate total change in the corresponding cell parameter. Some of the smaller nonzero 150 K values were rounded to zero. For example, the pseudo-linear slope of the $\Delta c(s_2)$ curve is −3.061 Å, so that a value of s_2 = +0.0169 (at 150 K) results in a change of $\Delta c \approx$ (−3.061 Å)(0.0169) = −0.052 Å, in addition to $\Delta\alpha = \Delta\beta \approx (+1.050)(0.0169)(180°/\pi) = +1.019°$.

longer be ignored. A simple phenomenological description of such a coupling is described in the SI.

What is it about the CA-Pyz structure that causes the $\Gamma_2^+-\Gamma_1^+$ strain coupling to increase below ~260 K? The structural distortions in CA-Pyz are best understood with respect to the H-bonded chains, which run along the child-cell's body diagonal ([110] of the parent) and are emphasized by red and blue shading in Figure 5. Rotational symmetry-mode refinement shows that the main structural change is a cooperative rotation of all Pyz molecules in the $z = 0$ plane, which occurs around an axis close to the H···N(Pyz)N···H hydrogen bond direction (animations available in the SI). This is dominated by the r_4 Γ_2^+ rotation, with the smaller r_5 Γ_2^+ contribution acting to bring the rotation vector in line with the H-bonded chain. The significant shift in Pyz positions driven by the rotation couples with a sliding of adjacent planes of CA molecules, with each layer moving laterally from its high-temperature position by ~1 Å between 300 and 250 K. This is enabled by the relatively weak van der Waals interactions between CA planes and leads to the significant expansion of the *b*-axis on cooling. In addition to the dominant Γ_2^+ rotations, we see a small r_6 Γ_1^+ rotation below 260 K (shown with squares in Figure 4a). This corresponds (Figures 1 and 5) to a rotation of Pyz around an axis perpendicular to the N−N direction and in the plane of the ring. This motion "buckles" the CA-Pyz chain, causing a reduction in the *c* axis (~0.2 Å) and a small expansion on cooling in the *ab* plane (~0.1 Å increase in $\sqrt{ab\,\sin(\gamma)}$ as an in-plane measure of the dimension) as the Pyz plane becomes more closely aligned with it. It seems likely that this distortion occurs as a result of the large r_4 rotation and provides the observed coupling between Γ_2^+ and Γ_1^+ strains that emerges with the decreasing temperature.

CONCLUSIONS

Our variable temperature single-crystal and powder diffraction studies have shown that CA-Pyz undergoes a reversible phase transition close to room temperature, which leads to extreme anisotropy in thermal expansion and a remarkable 14% size reduction in one dimension over a 100 K range. The effects of the transition are seen over a ~150 to 300 K temperature range. Highly anisotropic thermal expansion coefficients up to +1500 and -1500×10^{-6} K^{-1} result. These occur over a significant temperature range close to room temperature and without any external driving effects such as spin crossover or composition change. In the HT form, anisotropic atomic displacement parameters derived from neutron diffraction data suggest significant (~22°) librational disorder of pyrazine molecules around an axis defined by the H···N(Pyz)N···H hydrogen bonds, which freeze out as a ~16° static rotation on cooling. The transition, which is presumably entropically driven, is enabled by the cooperative sliding of adjacent molecular layers by ~1 Å and leads to the high thermal anisotropy. It, thus, has similarities to the alkyl-chain disorder reported in a Co complex,[64] which leads to cell parameter changes of +8/−5% at a first-order transition, and to the abrupt uniaxial contraction caused by oxalate reorientation in $[\mathrm{Ni^{II}(en)_3}](\mathrm{ox})$.[65] It differs from these examples in that the transition is second-order-like and occurs over a broad temperature range. The cooperative nature of the structural change, which involves relatively small displacements of adjacent layers, and the relationship between the parent and child cells is reminiscent of a diffusionless martensitic transition. It is, therefore, likely that a similar change can be stress-induced, potentially leading to phenomena such as superelasticity or shape memory. Extreme cell parameter changes are often associated with martensitic transitions. For example, the transitions in NiTi and the organic superelastic terephthalamide[13] correspond to respective cell parameter changes approaching ±10 and ±7%.

This work also shows that rotational symmetry modes provide a powerful symmetry-derived description of the phase transition in CA-Pyz, allowing us to describe the essence of the structural changes in a small number of parameters, principally a Γ_2^+ strain and rotation. The use of strain modes to describe thermal expansion also allows us to understand the unusual temperature dependence of cell parameters in this material in terms of coupling between primary and secondary order parameters. These methods can be used for a wide range of molecular and hybrid materials undergoing phase transitions and can be readily applied using the ISODISTORT and TOPAS approaches, allowing useful information to be determined on such materials even using relatively low-quality powder diffraction data.

ASSOCIATED CONTENT

Supporting Information

The Supporting Information is available free of charge on the ACS Publications website at DOI: 10.1021/acs.chemmater.9b01135.

Influence of secondary mode coupling on thermal expansion; laboratory powder diffraction data showing the phase transition; microstrain peak shape parameters; cell parameter data from single-crystal experiments and in alternate cell settings; selected bond lengths from single-crystal experiments, plots of anisotropic displacement parameters; ^{1}H solid-state NMR data (PDF)

Crystollagraphic data (CIF) (CIF) (CIF) (CIF) (CIF) (CIF)

Animations of key distortions (MOV) (MOV) (MOV)

AUTHOR INFORMATION

Corresponding Authors

*E-mail: ivana.radosavljevic@durham.ac.uk (I.R.E.).
*E-mail: john.evans@durham.ac.uk (J.S.O.E.).

ORCID

Huiyu Liu: 0000-0003-1725-6056
Ivana Radosavljevic Evans: 0000-0002-0325-7229

Author Contributions

All authors have given approval to the final version of the manuscript.

Notes

The authors declare no competing financial interest.

ACKNOWLEDGMENTS

We thank Dr David Apperley of the Durham Solid State NMR service. I.R.E. acknowledges the Royal Society and the Leverhulme Trust for the award of a Senior Research Fellowship (SRF/R1/180040).

ABBREVIATIONS

CA, chloranilic acid; Pyz, pyrazine

REFERENCES

(1) Sato, O. Dynamic molecular crystals with switchable physical properties. *Nat. Chem.* **2016**, *8*, No. 644.

(2) Ahmed, E.; Karothu, D. P.; Naumov, P. Crystal adaptronics: mechanically reconfigurable elastic and superelastic molecular crystals. *Angew. Chem., Int. Ed.* **2018**, *57*, 8837−8846.

(3) Naumov, P.; Chizhik, S.; Panda, M. K.; Nath, N. K.; Boldyreva, E. Mechanically Responsive Molecular Crystals. *Chem. Rev.* **2015**, *115*, 12440−12490.

(4) Reddy, C. M.; Rama Krishna, G.; Ghosh, S. Mechanical properties of molecular crystals—applications to crystal engineering. *CrystEngComm* **2010**, *12*, 2296−2314.

(5) Sahoo, S. C.; Panda, M. K.; Nath, N. K.; Naumov, P. Biomimetic Crystalline Actuators: Structure−Kinematic Aspects of the Self-Actuation and Motility of Thermosalient Crystals. *J. Am. Chem. Soc.* **2013**, *135*, 12241−12251.

(6) Kaneko, F.; Kobayashi, M.; Sato, K.; Suzuki, M. Martensitic phase transition of petroselinic acid: Influence of polytypic structure. *J. Phys. Chem. B* **1997**, *101*, 285−292.

(7) Davey, R. J.; Maginn, S. J.; Andrews, S. J.; Black, S. N.; Buckley, A. M.; Cottier, D.; Dempsey, P.; Plowman, R.; Rout, J. E.; Stanley, D. R.; Taylor, A. Morphology and polymorphism in molecular-crystals - terephthalic acid. *J. Chem. Soc., Faraday Trans.* **1994**, *90*, 1003−1009.

(8) Parkinson, G. M.; Thomas, J. M.; Williams, J. O.; Goringe, M. J.; Hobbs, L. W. Suggested role of partial dislocations in single-crystal reversible single-crystal phase-transition of a cyclo-octatne molecular cationic salt. *J. Chem. Soc., Perkin Trans. 2* **1976**, 836−838.

(9) Jones, W.; Thomas, J. M.; Williams, J. O. Electron and optical microscopic studies of a stress-induced phase transition in 1,8-dichloro-10-methylanthracene. *Philos. Mag. A* **1975**, *32*, 1−11.

(10) Kaneko, F.; Yano, J.; Tsujiuchi, H.; Tashiro, K.; Suzuki, M. Two Martensitic Transitions in the Opposite Directions in Pentadecanoic Acid. *J. Phys. Chem. B* **1998**, *102*, 327−330.

(11) Karothu, D. P.; Weston, J.; Desta, I. T.; Naumov, P. Shape-Memory and Self-Healing Effects in Mechanosalient Molecular Crystals. *J. Am. Chem. Soc.* **2016**, *138*, 13298−13306.

(12) Jones, W.; Williams, J. O. Real Space Crystallography and defects in molecular crystals. *J, Mater. Sci.* **1975**, *10*, 379−386.

(13) Takamizawa, S.; Miyamoto, Y. Superelastic Organic Crystals. *Angew. Chem., Int. Ed.* **2014**, *53*, 6970−6973.

(14) Takamizawa, S.; Takasaki, Y. Shape-memory effect in an organosuperelastic crystal. *Chem. Sci.* **2016**, *7*, 1527−1534.

(15) Suzuki, I.; Okada, K. Direct observation of ferroelasticity in squaric acid $C_4H_2O_4$. *Solid State Commun.* **1979**, *29*, 759−762.

(16) Schwenk, H.; Neumaier, K.; Andres, K.; Wudl, F.; Aharonshalom, E. Meissner anisotropy in deuterated $(TMTSF)_2ClO_4$. *Mol. Cryst. Liq. Cryst.* **1982**, *79*, 277−282.

(17) Mukoujima, M.; Kawabata, K.; Sambongi, T. Unusual motion of twin boundary in $(TMTSF)_2PF_6$ single crystal under constant stress. *Solid State Commun.* **1996**, *98*, 283−286.

(18) Williams-Seton, L.; Davey, R. J.; Lieberman, H. F.; Pritchard, R. G. Disorder and twinning in molecular crystals: Impurity-induced effects in adipic acid. *J. Pharm. Sci.* **2000**, *89*, 346−354.

(19) Bandyopadhyay, R.; Grant, D. J. W. Plasticity and slip system of plate-shaped crystals of L-lysine monohydrochloride dihydrate. *Pharm. Res.* **2002**, *19*, 491−496.

(20) Reddy, C. M.; Kirchner, M. T.; Gundakaram, R. C.; Padmanabhan, K. A.; Desiraju, G. R. Isostructurality, polymorphism and mechanical properties of some hexahalogenated benzenes: The nature of halogen center dot center dot center dot halogen interactions. *Chem. - Eur. J.* **2006**, *12*, 2222−2234.

(21) Mir, S. H.; Takasaki, Y.; Engel, E. R.; Takamizawa, S. Ferroelasticity in an Organic Crystal: A Macroscopic and Molecular Level Study. *Angew. Chem., Int. Ed.* **2017**, *56*, 15882−15885.

(22) Takamizawa, S.; Takasaki, Y.; Sasaki, T.; Ozaki, N. Superplasticity in an organic crystal. *Nat. Commun.* **2018**, *9*, No. 3984.

(23) Herbstein, F. H. On the mechanism of some first-order enantiotropic solid-state phase transitions: from Simon through Ubbelohde to Mnyukh. *Acta Crystallogr., Sect. B: Struct. Sci.* **2006**, *62*, 341−383.

(24) White, G. K. Solids: Thermal expansion and contraction. *Cont. Phys.* **1993**, *34*, 193−204.

(25) Mary, T. A.; Evans, J. S. O.; Vogt, T.; Sleight, A. W. Negative Thermal Expansion from 0.3 to 1050 Kelvin in ZrW_2O_8. *Science* **1996**, *272*, 90−92.

(26) Evans, J. S. O.; Mary, T. A.; Sleight, A. W. Negative Thermal Expansion in $Sc_2(WO_4)_3$. *J. Sol. State Chem.* **1998**, *137*, 148−160.

(27) Lightfoot, P.; Woodcock, D. A.; Maple, M. J.; Villaescusa, L. A.; Wright, P. A. The widespread occurrence of negative thermal expansion in zeolites. *J. Mater. Chem.* **2001**, *11*, 212−216.

(28) Evans, J. S. O. Negative Thermal Expansion Materials. *Jpn. J. Appl. Phys.* **2000**, *39*, No. 535.

(29) Goodwin, A. L.; Calleja, M.; Conterio, M. J.; Dove, M. T.; Evans, J. S. O.; Keen, D. A.; Peters, L.; Tucker, M. G. Colossal Positive and Negative Thermal Expansion in the Framework Material $Ag_3[Co(CN)_6]$. *Science* **2008**, *319*, 794−797.

(30) Cliffe, M. J.; Hill, J. A.; Murray, C. A.; Coudert, F.-X.; Goodwin, A. L. Defect-dependent colossal negative thermal expansion in UiO-66(Hf) metal-organic framework. *Phys. Chem. Chem. Phys.* **2015**, *17*, 11586−11592.

(31) Mullaney, B. R.; Goux-Capes, L.; Price, D. J.; Chastanet, G.; Létard, J.-F.; Kepert, C. J. Spin crossover-induced colossal positive and negative thermal expansion in a nanoporous coordination framework material. *Nat. Commun.* **2017**, *8*, No. 1053.

(32) Commins, P.; Desta, I. T.; Karothu, D. P.; Panda, M. K.; Naumov, P. Crystals on the move: mechanical effects in dynamic solids. *Chem. Commun.* **2016**, *52*, 13941−13954.

(33) Panda, M. K.; Runčevski, T.; Chandra Sahoo, S.; Belik, A. A.; Nath, N. K.; Dinnebier, R. E.; Naumov, P. Colossal positive and negative thermal expansion and thermosalient effect in a pentamorphic organometallic martensite. *Nat. Commun.* **2014**, *5*, No. 4811.

(34) Panda, M. K.; Centore, R.; Causà, M.; Tuzi, A.; Borbone, F.; Naumov, P. Strong and Anomalous Thermal Expansion Precedes the Thermosalient Effect in Dynamic Molecular Crystals. *Sci. Rep.* **2016**, *6*, No. 29610.

(35) Das, D.; Jacobs, T.; Barbour, L. J. Exceptionally large positive and negative anisotropic thermal expansion of an organic crystalline material. *Nat. Mater.* **2010**, *9*, 36−39.

(36) Fortes, A. D.; Suard, E.; Knight, K. S. Negative linear compressibility and massive anisotropic thermal expansion in methanol monohydrate. *Science* **2011**, *331*, 742−746.

(37) Altomare, A. C. G.; Giacovazzo, C.; Guagliardi, A.; Burla, M. C.; Polidori, G.; Camalli, M.; et al. SIR92. *J. Appl. Crystallogr.* **1994**, *27*, No. 435.

(38) Betteridge, P. W.; Carruthers, J. R.; Cooper, R. I.; Prout, K.; Watkin, D. J. CRYSTALS. *J. Appl. Crystallogr.* **2003**, *36*, No. 1487.

(39) Petříček, V.; Dušek, M.; Palatinus, L. Crystallographic Computing System JANA2006: General features. *Z. Kristallogr. - Cryst. Mater.* **2014**, *229*, 345−352.

(40) Spek, A. Structure validation in chemical crystallography. *Acta Crystallogr., Sect. D: Biol. Crystallogr.* **2009**, *65*, 148−155.

(41) Dinnebier Robert, E.; Leineweber, A.; Evans John, S. O. *Rietveld Refinement, Practical Powder Diffraction Pattern Analysis using TOPAS*; Walter de Gruyter GmbH & Co KG, 2019.

(42) Coelho, A. TOPAS and TOPAS-Academic: an optimization program integrating computer algebra and crystallographic objects written in C++. *J. Appl. Crystallogr.* **2018**, *51*, 210−218.

(43) Coelho, A. A.; Evans, J. S. O.; Evans, I. R.; Kern, A.; Parsons, S. The TOPAS symbolic computation system. *Powder Diffraction* **2011**, *26*, No. S22.

(44) Campbell, B. J.; Stokes, H. T.; Tanner, D. E.; Hatch, D. M. ISODISPLACE: a web-based tool for exploring structural distortions. *J. Appl. Crystallogr.* **2006**, *39*, 607−614.

(45) Pawley, G. Unit-cell refinement from powder diffraction scans. *J. Appl. Crystallogr.* **1981**, *14*, 357−361.

(46) Jarvinen, M. Application of symmetrized harmonics expansion to correction of the preferred orientation effect. *J. Appl. Crystallogr.* **1993**, *26*, 525−531.

(47) Loiseau, T.; Serre, C.; Huguenard, C.; Fink, G.; Taulelle, F.; Henry, M.; Bataille, T.; Férey, G. A Rationale for the Large Breathing of

the Porous Aluminum Terephthalate (MIL-53) Upon Hydration. *Chem. - Eur. J.* **2004**, *10*, 1373−1382.

(48) Liu, Y.; Her, J.-H.; Dailly, A.; Ramirez-Cuesta, A. J.; Neumann, D. A.; Brown, C. M. Reversible Structural Transition in MIL-53 with Large Temperature Hysteresis. *J. Am. Chem. Soc.* **2008**, *130*, 11813−11818.

(49) Ishida, H.; Kashino, S. 1:1 Complexes of chloranilic acid with pyrazine and morpholine: one- and two-dimensional hydrogen-bond networks. *Acta Crystallogr., Sect. C: Cryst. Struct. Commun.* **1999**, *55*, 1923−1926.

(50) Steiner, T. The Hydrogen Bond in the Solid State. *Angew. Chem., Int. Ed.* **2002**, *41*, 48−76.

(51) Ford, S. J.; Delamore, O. J.; Evans, J. S. O.; McIntyre, G. J.; Johnson, M. R.; Radosavljević Evans, I. Giant Deuteron Migration During the Isosymmetric Phase Transition in Deuterated 3,5-Pyridinedicarboxylic Acid. *Chem. - Eur. J.* **2011**, *17*, 14942−14951.

(52) Schomaker, V.; Trueblood, K. N. On the rigid-body motion of molecules in crystals. *Acta Crystallogr., Sect. B: Struct. Crystallogr. Cryst. Chem.* **1968**, *24*, 63−76.

(53) Lewis, J. W.; Payne, J. L.; Evans, I. R.; Stokes, H. T.; Campbell, B. J.; Evans, J. S. O. An Exhaustive Symmetry Approach to Structure Determination: Phase Transitions in $Bi_2Sn_2O_7$. *J. Am. Chem. Soc.* **2016**, *138*, 8031−8042.

(54) Stroppa, A.; Barone, P.; Jain, P.; Perez-Mato, J. M.; Picozzi, S. Hybrid Improper Ferroelectricity in a Multiferroic and Magnetoelectric Metal-Organic Framework. *Adv. Mater.* **2013**, *25*, 2284−2290.

(55) Kerman, S.; Campbell, B. J.; Satyavarapu, K. K.; Stokes, H. T.; Perselli, F.; Evans, J. S. O. The superstructure determination of displacive distortions via symmetry-mode analysis. *Acta Crystallogr., Sect. A: Found. Crystallogr.* **2012**, *68*, 222−234.

(56) Campbell, B.; Evans, J.; Perselli, F.; Stokes, H. Rietveld refinement of structural distortion-mode amplitudes. *IUCr Cryst. Comp. Newsletter* **2007**, *8*, 81−95.

(57) Orobengoa, D.; Capillas, C.; Aroyo, M. I.; Perez-Mato, J. M. AMPLIMODES: symmetry-mode analysis on the Bilbao Crystallographic Server. *J. Appl. Crystallogr.* **2009**, *42*, 820−833.

(58) Etter, M.; Müller, M.; Dinnebier, R. E. Rotational Rigid Body Symmetry Modes: A Tool for the Investigation of Phase Transitions. *Z. Anorg. Allg. Chem.* **2014**, *640*, 3079−3087.

(59) Müller, M.; Dinnebier, R. E.; Dippel, A.-C.; Stokes, H. T.; Campbell, B. J. A symmetry-mode description of rigid-body rotations in crystalline solids: a case study of $Mg(H_2O)_6RbBr_3$. *J. Appl. Crystallogr.* **2014**, *47*, 532−538.

(60) Liu, H.; Zhang, W.; Halasyamani, P. S.; Stokes, H. T.; Campbell, B. J.; Evans, J. S. O.; Evans, I. R. Understanding the Behavior of the Above-Room-Temperature Molecular Ferroelectric 5, 6-Dichloro-2-methylbenzimidazole Using Symmetry Adapted Distortion Mode Analysis. *J. Am. Chem. Soc.* **2018**, *140*, 13441−13448.

(61) Campbell, B.; Howard, C. J.; Averett, T. B.; Whittle, T. A.; Schmid, S.; Machlus, S.; Yost, C.; Stokes, H. T. An algebraic approach to cooperative rotations in networks of interconnected rigid units. *Acta Crystallogr., Sect. A: Found. Adv.* **2018**, *74*, 408−424.

(62) Uddin, M. J.; Middya, T. R.; Chaudhuri, B. K. Room temperature ferroelectric effect and enhanced dielectric permittivity in Rochelle salt/PVA percolative composite films. *Curr. Appl. Phys.* **2013**, *13*, 461−466.

(63) Busing, W. R.; Levy, H. A. The effect of thermal motion on the estimation of bond lengths from diffraction measurements. *Acta. Cryst.* **1964**, *17*, 142−146.

(64) Su, S.-Q.; Kamachi, T.; Yao, Z.-S.; Huang, Y.-G.; Shiota, Y.; Yoshizawa, K.; Azuma, N.; Miyazaki, Y.; Nakano, M.; Maruta, G.; et al. Assembling an alkyl rotor to access abrupt and reversible crystalline deformation of a cobalt (II) complex. *Nat. Commun.* **2015**, *6*, No. 8810.

(65) Yao, Z.-S.; Mito, M.; Kamachi, T.; Shiota, Y.; Yoshizawa, K.; Azuma, N.; Miyazaki, Y.; Takahashi, K.; Zhang, K.; Nakanishi, T.; et al. Molecular motor-driven abrupt anisotropic shape change in a single crystal of a Ni complex. *Nat. Chem.* **2014**, *6*, No. 1079.